Interfacing topological insulators and ferrimagnets: Bi_2Te_3 and Fe_3O_4 heterostructures grown by molecular beam epitaxy

V.M. Pereira,[1, a)] C.N. Wu,[1, 2] C.-A. Knight,[1, 3] A. Choa,[1, 3] L.H. Tjeng,[1] and S.G. Altendorf[1]
[1)] *Max Planck Institute for Chemical Physics of Solids, Nöthnitzer Str. 40, 01187 Dresden, Germany*
[2)] *Department of Physics, National Tsing Hua University, Hsinchu 30013, Taiwan*
[3)] *Department of Physics and Astronomy, University of British Columbia, Vancouver, BC V6T 1Z1, Canada*

(Dated: 12 March 2024)

Relying on the magnetism induced by the proximity effect in heterostructures of topological insulators and magnetic insulators is one of the promising routes to achieve the quantum anomalous Hall effect. Here we investigate heterostructures of Bi_2Te_3 and Fe_3O_4. By growing two different types of heterostructures by molecular beam epitaxy, Fe_3O_4 on Bi_2Te_3 and Bi_2Te_3 on Fe_3O_4, we explore differences in chemical stability, crystalline quality, electronic structure, and transport properties. We find the heterostructure Bi_2Te_3 on Fe_3O_4 to be a more viable approach, with transport signatures in agreement with a gap opening in the topological surface states.

I. INTRODUCTION

Since its initial theoretical prediction[1], topological insulators (TIs) like the prototypical Bi_2Te_3 and Bi_2Se_3 have been extensively studied due to the multitude of features stemming from their topological surface states. Many of the recent studies on TIs have concentrated on breaking the time reversal symmetry by introducing magnetic order in the system, as this can lead to exotic phenomena such as the quantum anomalous Hall effect (QAHE). Requisite to this is the opening of a gap in the topological surface states, which can be experimentally achieved either by magnetic doping of the TI[2–5] or by making use of the magnetic proximity effect at the interface between a TI and a magnetic layer[6–9]. Although magnetic doping has been proven to be an effective approach and the QAHE has been observed for these systems[2], the magnetic proximity effect can carry significant advantages. In addition to the much higher Curie temperature of the magnetic layer, one can avoid the inherent inhomogeneity of the doping process and additional scattering processes that reduce the mobility. One can also achieve a uniform magnetization at the interface between the TI and the magnetic layer. This could lead to an increase of the temperature for which the QAHE is observed, surpassing the low temperatures of less than 2 K[2–4] that are currently necessary for magnetically doped TI systems.

Earlier studies of interfaces between TIs and ferromagnets focused on the use of Fe as an adlayer[10–14]. However, several studies found that the interface of Fe/TI is not clean, and that the Fe atoms penetrate into the TI layer, forming an interface layer containing FeTe or FeSe[13,14]. Since any possible applications of these heterostructures for spintronic devices rely on well-defined interfaces, it is crucial to have a sharp interface, without chemical reactions between the layers. For this purpose, magnetic transition metal oxide insulators are promising candidates, due to their relatively inert nature when compared to the magnetic transition metals themselves. Being insulators, these will not contribute to the conductivity and, as a result, unambiguous monitoring of the topological surface states can be readily achieved.

In this work, we have selected Fe_3O_4 (magnetite) and Bi_2Te_3 as our respective magnetic layer and TI. Magnetite is an extensively investigated ferrimagnet owing to its interesting electrical and magnetic properties, from which we emphasize the high Curie temperature around 860 K. It also has a characteristic first-order metal-insulator transition occurring at 124 K, known as the Verwey transition[15]. We have chosen Fe_3O_4 because the detailed growth conditions, needed to obtain high quality films, have been recently established by Liu *et al.*[16,17]. Bi_2Te_3 was selected as the TI because it has been demonstrated by Höfer *et al.*[18] that stoichiometric films of Bi_2Te_3 can be grown, which are truly insulating in their bulk and show only intrinsic surface conductivity. Here we investigate the interface between these materials. We study the transport properties of the heterostructures to detect the presence of the proximity effect. The opening of an exchange gap in the TI surface states will lead to a suppression of the weak anti-localization (WAL) effect, a characteristic of TIs, and will induce the weak localization (WL) effect[7,9,19,20]. Here we note that for the case of Bi_2Te_3 the QAHE can be induced not only by an out-of-plane magnetization but also by an in-plane magnetization due to the warping effects of the topological surface states[21,22], giving us more flexibility in the choice of the magnetic material and interface.

The present work reports on two different heterostructures of Bi_2Te_3 and Fe_3O_4, namely Fe_3O_4 / Bi_2Te_3 / Al_2O_3 (0001) and Bi_2Te_3 / Fe_3O_4 / MgO (001). These were characterized *in situ* by reflection high-energy electron diffraction, x-ray photoelectron spectroscopy,

[a)] Electronic mail: vanda.pereira@cpfs.mpg.de

and angle-resolved photoelectron spectroscopy. We then present the transport properties of these heterostructures and discuss the findings.

II. EXPERIMENT

The films were prepared by molecular beam epitaxy (MBE) in an *in situ* system with base pressure of about 2×10^{-10} mbar. This comprises two MBE growth chambers, one dedicated to Bi_2Te_3 and the other to Fe_3O_4.

For the investigation of Fe_3O_4 on Bi_2Te_3, the heterostructure described in the first part of this manuscript, Bi_2Te_3 films were grown on Al_2O_3 (0001) substrates purchased from Crystec GmbH. Prior to the deposition, the substrates were annealed at 600 °C for 2 hours in an oxygen pressure of 1×10^{-6} mbar. High purity Bi and Te were evaporated from effusion cells with flux rates measured by a quartz crystal monitor at the growth position. The flux rates were set at 0.5 Å/min for Bi ($T_{Bi} \approx 458$ °C) and 1.5 Å/min for Te ($T_{Te} \approx 228$ °C). Bi_2Te_3 was grown in a two-step procedure. First, 3 quintuple layers (QLs) were deposited at 160 °C and annealed at 240 °C in Te atmosphere for 30 minutes. Then, we deposited 7 more QLs at 220 °C, amounting to a final thickness of 10 QLs (see also Ref. 18). Subsequently, Fe was evaporated at temperatures of about 1185 - 1230 °C (flux rate of Fe, ϕ_{Fe} = 0.5 - 1 Å/min) in a pure oxygen atmosphere on top of the Bi_2Te_3 layer. Molecular oxygen was supplied through a leak valve, varying the partial pressure, P_{Ox}, between 5×10^{-8} and 1×10^{-5} mbar.

For the heterostructure with Bi_2Te_3 on Fe_3O_4, described in the second part, 30 nm-thick Fe_3O_4 films were grown on MgO (001) substrates purchased from Crystec GmbH, following the recipe from Refs. 16, 17, and 23. Subsequently, Bi_2Te_3 was deposited on top, using a slightly modified two-step procedure.

Reflection high-energy electron diffraction (RHEED) was used to monitor in *real-time* the epitaxial growth, using a STAIB Instruments RH35 system with the kinetic energy of the electrons set at 15 keV (Bi_2Te_3) or 20 keV (Fe_3O_4). All samples were characterized *in situ* by x-ray photoelectron spectroscopy (XPS) using monochromatized Al K_α light (1486.6 eV) and angle-resolved photoelectron spectroscopy (ARPES) using a non-monochromatic He discharge lamp with 21.2 eV photon energy (He I line) at room temperature and using a Scienta R3000 electron energy analyzer.

In order to characterize the structural quality of the films, *ex situ* x-ray diffraction (XRD) measurements were performed with a PANalytical XPert PRO diffractometer using monochromatic Cu-$K_{\alpha1}$ radiation ($\lambda = 1.54056$ Å). Atomic force microscopy (AFM) was carried out using a Veeco Metrology MultiMode Atomic Force Microscope (Model 920-006-101) in tapping mode.

To avoid the contamination of Bi_2Te_3 during *ex situ* transport measurements, the heterostructure with Bi_2Te_3 on Fe_3O_4 was capped *in situ* with 12 nm of Te grown at room temperature[24] prior to the transfer to outside of the UHV system. Electrodes and connections were made of cut and pressed indium balls and copper wires in a standard Van der Pauw configuration. Transport measurements were performed using a Physical Property Measurement System from Quantum Design with a base temperature of 2 K.

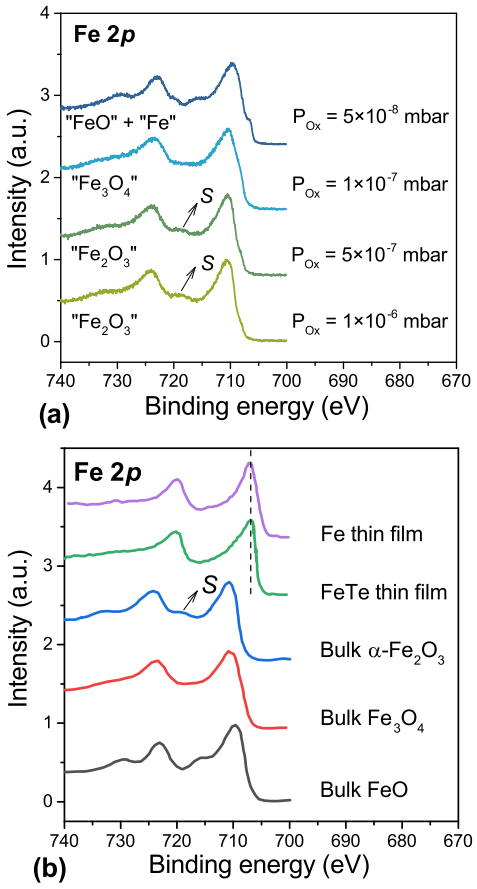

FIG. 1. (a) Fe 2*p* XPS spectra of nominally 40-nm-thick FeO_x films grown on 10 QL Bi_2Te_3 at 50-55 °C substrate temperature and $\phi_{Fe} = 1$ Å/min under various oxygen pressures. The resulting phase is indicated by the labels in quotation marks. (b) Reference Fe 2*p* XPS spectra of Fe and FeTe thin films (reproduced from Ref. 25) and bulk α-Fe_2O_3, Fe_3O_4 and FeO (reproduced from Ref. 26).

III. RESULTS AND DISCUSSION

A. Fe_3O_4 on Bi_2Te_3 on Al_2O_3 (0001)

For all the films in the current subsection, 10 QLs of Bi_2Te_3 were deposited onto Al_2O_3 (0001) substrates as described in the Experiment section. Afterwards, Fe was deposited in an oxygen atmosphere, varying the growth parameters such as the flux rate of Fe and the oxygen partial pressure. The parameters were optimized in order

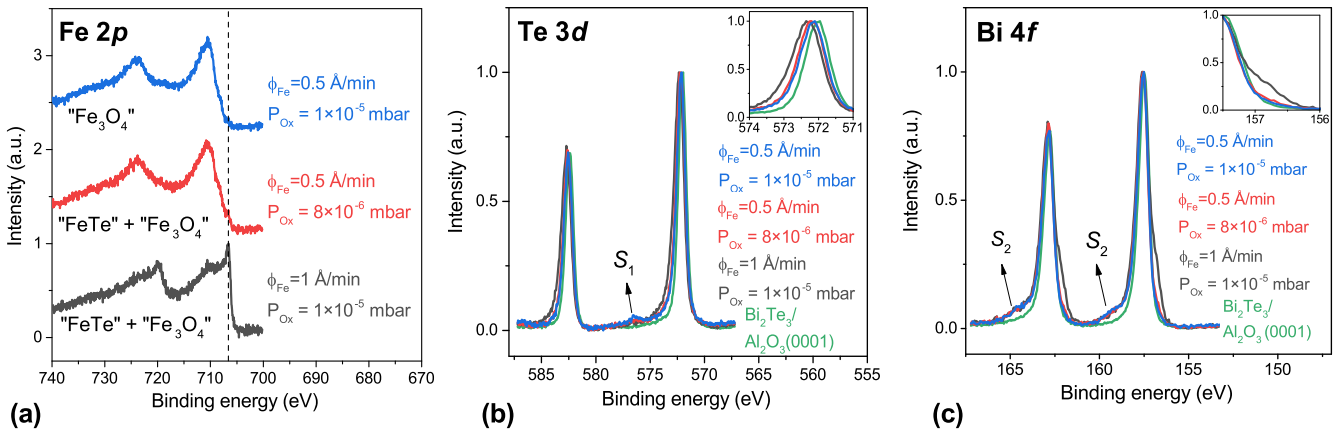

FIG. 2. XPS spectra of the Fe $2p$ (a), Te $3d$ (b) and Bi $4f$ (c) core levels for various ratios of Fe to O_2, for a nominal thickness of 6 MLs of FeO_x on top of 10 QLs of Bi_2Te_3. The resulting phases are indicated by the labels in quotation marks. For (b) and (c), the reference XPS spectra of a 10 QL Bi_2Te_3 thin film grown on Al_2O_3 (0001) are shown in green. The insets show a closeup of the Te $3d$ and Bi $4f$ peaks.

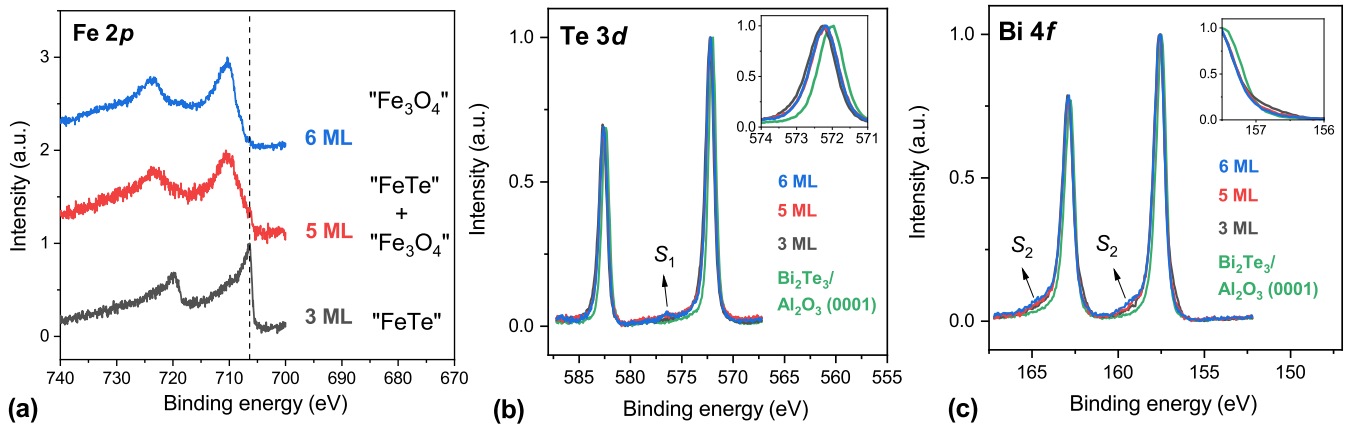

FIG. 3. XPS spectra of the Fe $2p$ (a), Te $3d$ (b) and Bi $4f$ (c) core level for various nominal thicknesses of FeO_x on top of 10 QLs of Bi_2Te_3. The Fe flux rate and oxygen pressure were kept constant at 0.5 Å/min and 1×10^{-5} mbar, respectively. The resulting phases are indicated by the labels in quotation marks. For (b) and (c), the reference XPS spectra of a 10 QL Bi_2Te_3 thin film grown on Al_2O_3 (0001) are shown in green.

to avoid strong chemical reactions between the layers and ultimately achieve a satisfactory growth of Fe_3O_4. For all the films reported here, the substrate temperature ranged from 50-55 °C due to the radiation heat load from the Fe effusion cell in thermal equilibrium with the unheated sample holder. All attempts to grow Fe_3O_4 at higher temperatures led to strong chemical reactions with the TI layer.

Our first aim was to establish the optimal conditions required for a sustained growth of Fe_3O_4 films at this substrate temperature range. We began with the conditions that were found to be optimal for films grown on oxide substrates at 250 °C (Refs. 16, 17, and 23), namely an Fe flux rate of 1 Å/min with an oxygen partial pressure of 1×10^{-6} mbar. The bottom (light green) curve of Figure 1(a) shows the Fe $2p$ XPS spectrum of a nominally 40 nm FeO_x film grown under these conditions on 10 QLs of Bi_2Te_3. In Figure 1(b) we have also collected Fe $2p$ spectra of several reference Fe compounds, which include an Fe metal film (purple curve), FeTe film (green), Fe_2O_3 bulk (blue), Fe_3O_4 bulk (red), and FeO bulk (dark gray). We observe from the spectral line shape that the 40 nm FeO_x film (Fig. 1(a) light green) has all the characteristics of a Fe_2O_3-like phase (Fig. 1(b) blue), i.e. it is overoxidized, as is indicated by the presence of the satellite peak labeled S. We then lowered the oxygen pressure to 5×10^{-7} mbar and obtained a 40 nm FeO_x film (Fig. 1(a) dark green) that is also Fe_2O_3-like, with the S feature still present. Lowering the pressure even further to 1×10^{-7} mbar produces a film for which the Fe $2p$ spectrum (Fig. 1(a) light blue) is quite similar to that of Fe_3O_4 bulk (Fig. 1(b) red). Finally, with 5×10^{-8} mbar pressure, the Fe $2p$ spectrum of the film (Fig. 1(a) dark blue) shows features that belong to FeO

(Fig. 1(b) dark gray) and Fe metal (Fig. 1(b) purple). These results thus present a significant difference from the ones reported for the growth of magnetite on oxide substrates at temperatures of 250 °C (Refs. 16, 17, and 23). It appears that high substrate temperatures allow for a wide range of oxygen pressures leading to the formation of good quality magnetite films, while the lower temperature necessary for the growth on Bi_2Te_3 considerably narrows the growth window of magnetite.

In the next step, we investigated the growth process of FeO_x closer to the interface with the Bi_2Te_3 layer. To this end we prepared a series of samples with nominally 6 monolayers (MLs) of FeO_x using various ratios of Fe to oxygen (here given by the flux rate of Fe and oxygen partial pressure). For these thinner films, we observed that the relatively low oxygen pressures, similar to the ones used previously, led to strong Fe-Te reactions at the interface indicating the need for higher oxygen pressures for the growth of the Fe_3O_4 layer. However, even for a pressure of 1×10^{-5} mbar, we also observe that the Fe $2p$ spectrum of the resulting 6 ML film, as shown by the bottom curve (dark gray) in Figure 2(a), contains features that belong to a mixture of Fe_3O_4 and Fe metal and/or FeTe. Here we emphasize the presence of the intense peak at 707 eV binding energy, marked by the dashed line in Figure 2(a), that is characteristic for Fe metal or FeTe, indicated also by the dashed line in Fig. 1(b). A further comparison of the corresponding Te $3d$ and Bi $4f$ spectra with the reference 10 QL Bi_2Te_3 grown on Al_2O_3 (green curves) in Figures 2(b) and (c) shows a shift towards higher binding energies and a shoulder at lower binding energies, respectively, as seen in the insets. These results strongly indicate the presence of a reaction between both layers, leading to the formation of FeTe and the consequent appearance of metallic bismuth at 157 and 162 eV (Ref. 27).

Subsequently, we further increased the oxygen to Fe ratio. The red curve in Figure 2 uses an Fe flux rate of 0.5 Å/min and oxygen partial pressure of 8×10^{-6} mbar. The Fe $2p$ spectrum shows a considerable reduction of the peak at 707 eV, indicating less reaction between the FeO_x and Bi_2Te_3 layers. Indeed, the Te $3d$ and Bi $4f$ spectra are now more similar to the reference. Finally, the film prepared with Fe flux rate of 0.5 Å/min and oxygen partial pressure of 1×10^{-5} mbar (blue curve) presents the Fe $2p$ spectrum with much more similar features to the one expected for Fe_3O_4 (see Figure 1(b), red curve). The peak at 707 eV is no longer visible and no extra satellite peaks (indicative of the formation of FeO and Fe_2O_3 phases, for instance) can be observed. In addition to this, the Te $3d$ and Bi $4f$ core levels are more similar to the expected for Bi_2Te_3, indicating that the reactions between the layers are minimized. However, it should be noted that small amounts of tellurium and bismuth oxides are formed, as indicated by the small peaks/shoulders (S_1 and S_2) observed at higher binding energies on the Te $3d$ and Bi $4f$ spectra.

To obtain more information about the intricacies of the interface between FeO_x and Bi_2Te_3, we also studied the effect of the thickness of the Fe oxide layer for the thinnest films. To this end, the flux rate and oxygen partial pressure were kept constant, following the best results found in the previous experiment (ϕ_{Fe} = 0.5 Å/min and $P_{Ox} = 1\times10^{-5}$ mbar) and the nominal thickness was varied between 3 and 6 MLs. The Fe $2p$ XPS spectra are plotted in Figure 3(a). Rather than just the Fe/O_2 ratio, it can be noticed that also the nominal thickness is relevant for the successful growth of Fe_3O_4 on top of Bi_2Te_3. For very thin layers (gray curve), we observe a predominance of the Fe-Te bond (dashed line), while the Te $3d$ and Bi $4f$ spectra show similar trends to those reported in Figure 2, indicating the formation of FeTe and metallic Bi at the interface. It is possible that a significantly higher ratio of Fe to oxygen is needed in order to obtain Fe_3O_4 for such thin layers. However, the applied pressure is already near the limit of what can be tolerated in the MBE system. Nevertheless, as the nominal thickness is increased, Fe oxides start to form and, for 5 MLs, the presence of the peak at 707 eV is substantially reduced. Lastly, for 6 MLs the measured spectrum is very similar to that of Fe_3O_4. We note that the probing depth for 1486.6 eV photons is larger than the thicknesses of the films used here. Therefore, the signal from the first 3 MLs (Fe-Te bond) should still be observable for films with 5 and 6 MLs. The absence of the FeTe signal for thicker layers suggests that the thickness for a constant Fe/O_2 ratio is indeed one of the controlling factors.

From the results of this study, we conclude that the growth of Fe_3O_4 on top of Bi_2Te_3 is possible, but not perfect. To keep the reactions at the interface minimized, a two-step procedure was implemented: growing first 6 MLs with ϕ_{Fe} = 0.5 Å/min and $P_{Ox} = 1\times10^{-5}$ mbar and then growing up to 40 nm using an Fe flux rate of ϕ_{Fe} = 1 Å/min and lower oxygen pressure, $P_{Ox} = 1\times10^{-7}$ mbar, at a substrate temperature of roughly 50-55 °C.

Figure 4(a) depicts the RHEED patterns for the Bi_2Te_3 layer and the Fe oxide overlayer after each of the two steps of the growth. The streaky lines noticeable for 10 QLs of Bi_2Te_3 show the good quality of the topological insulator layer. Upon the growth of 6 MLs of magnetite, we have a predominance of an amorphous background where some lines/spots can be distinguished. For 40 nm of Fe_3O_4, the pattern shows rings and spots indicating a polycrystalline and possibly 3D growth.

The morphological characterization of 6 MLs of Fe_3O_4 on 10 QLs of Bi_2Te_3 on Al_2O_3 (0001) is depicted in Figure 4(b), as well as a reference TI film with 10 QLs (c). The AFM pictures show that the magnetite layer covers the Bi_2Te_3 in a relatively uniform manner, and the pyramid structures with 1 QL-steps, typical of Bi_2Te_3, can still be observed.

To search for the possible presence of the magnetic proximity effect, we conducted temperature-dependent resistance measurements, depicted in Figure 5(a). The same figure also shows the sheet resistance of a 10 QL TI thin film grown on Al_2O_3 (0001) for comparison. Both

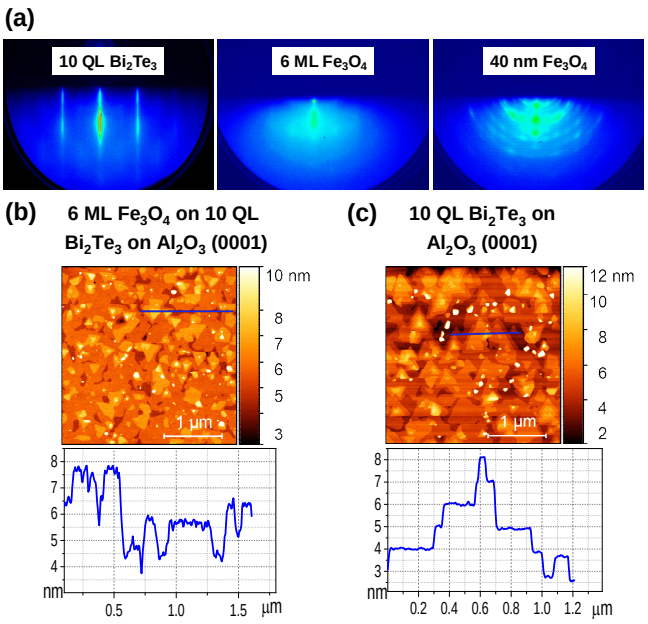

FIG. 4. (a) RHEED patterns of each step of the heterostructure: 10 QLs of Bi_2Te_3 on Al_2O_3 (0001) *(left)*; 6 MLs of Fe_3O_4 grown with $\phi_{Fe} = 0.5$ Å/min and $P_{Ox} = 1\times10^{-5}$ mbar *(center)* and 40 nm of Fe_3O_4 with $\phi_{Fe} = 1$ Å/min and $P_{Ox} = 1\times10^{-7}$ mbar *(right)*. (b) Morphological characterization by AFM of 6 MLs of Fe_3O_4 on 10 QLs of Bi_2Te_3 on Al_2O_3 (0001), (c) 10 QLs of Bi_2Te_3 on Al_2O_3 (0001). The blue lines in the AFM pictures represent the locations of the height profiles plotted below.

curves present quite similar features, with a metallic-like behavior, typical of the topological surface states, being predominant over the majority of the temperature range; for low temperatures, an upturn characteristic of TIs is observed. However, the absolute value of the sheet resistance diminishes considerably for the heterostructure. The formation of bismuth and tellurium oxides, observed by XPS, and some residual FeTe at the interface, can lead to doping of the TI due to Te vacancies and antisite defects, thus increasing the contribution of the bulk to the transport properties and decreasing the overall resistance. Moreover, considering a parallel resistance between the layers of Bi_2Te_3 and Fe_3O_4, it would be expected that the sheet resistance would be dominated by the magnetite signal above the Verwey transition temperature (for 40 nm Fe_3O_4 on MgO (001), the sheet resistance is $\approx$ 1200 Ω/sq at room temperature and the Verwey transition occurs at $T_V \approx 119$ K, cf. Ref. 16). When $T < T_V$, the magnetite layer is expected to be much more insulating and therefore the TI should be the main contributor to the resistance. The absence of the Verwey transition in this heterostructure, combined with the low crystalline order observed from RHEED, hints towards a subpar quality of the magnetite layer.

One possibility is that Bi and/or Te constituents are incorporated into the magnetite, leading to the formation of doped Fe_3O_4 and therefore suppressing the characteristic Verwey transition. Furthermore, the XPS sensitivity is a limiting factor on the identification of phases. It is also conceivable that the magnetite overlayer might contain small amounts of parasitic phases correspondent to other iron oxides, as FeO and Fe_2O_3, which are below the detection limit of this technique. On the other hand, the absence of a clear Verwey transition has been frequently reported in the literature for Fe_3O_4 films[16,28]. Liu *et al.* have investigated this phenomenon and found out that the Verwey transition temperature is strongly dependent on the size of the Fe_3O_4 crystallites, i.e. it starts to rapidly decrease if the crystallite or domain size becomes smaller than about 70 nm[16]. Under these conditions the transition in a Fe_3O_4 film is no longer sharp, with the broadness determined by the distribution of the crystallite or domain sizes in the film. For 5 nm Fe_3O_4 films and thinner Liu *et al.* did not observe a Verwey transition at all[16]. For our heterostructure, the disordered RHEED patterns, with the presence of broad spots, can be an indication of reduced structural domain sizes. It is therefore conceivable that the subpar quality of the magnetite layer does not allow for the Verwey transition to occur.

Figure 5(b) shows the comparative magnetoconductance measurements for a reference 10 QL Bi_2Te_3 film grown on Al_2O_3 (0001) (top) and the heterostructure of 40 nm Fe_3O_4 / 10 QL Bi_2Te_3 / Al_2O_3 (0001) (bottom). The weak anti-localization (WAL), characteristic of TIs, is expected to dominate the magnetoconductance for low temperatures and low magnetic fields. Additionally, for the heterostructures containing a magnetic layer, the weak localization (WL) is expected to arise as a signature of a gap opening by magnetic ordering[9,19]. This behavior can be described by an approximation of the Hikami-Larkin-Nagaoka (HLN) formula[29], given by

$$\Delta G_{xx} = \alpha \frac{e^2}{\pi h}\left[\ln\left(\frac{B_\phi}{B}\right) - \psi\left(\frac{1}{2}+\frac{B_\phi}{B}\right)\right] + \beta B^2 \quad (1)$$

where $\Delta G_{xx} = G_{xx}(B) - G_{xx}(0)$, $\alpha \equiv \alpha_0 + \alpha_1$ is a pre-factor which describes both WL ($\alpha_0 < 0$) and WAL ($\alpha_1 = 1/2$ per independent topological transport channel), $B_\phi = h/(8\pi e l_\phi^2)$, B is the applied magnetic field, l_ϕ is the phase coherence length, ψ is the digamma function and β is the coefficient of the magnetic field. α, l_ϕ and β are used as fitting parameters of the HLN equation. In this report, we use one set of α and l_ϕ for all the fits.

The magnetoconductance for the reference sample grown on Al_2O_3 (0001), Figure 5(b)-top, shows the typical behavior for a TI. The pronounced cusp at low temperatures and low magnetic fields shows the predominance of the WAL effect and it can be fitted by equation (1). The results of the fit at different temperatures for the reference sample are shown in Figure 5(c). $\alpha = \alpha_1$ has the expected value of ≈ 0.5 for the lowest measured temperature, indicating the presence of one conducting channel, since the top and bottom conducting channels are coupled through the bulk carriers in the thin layer[30].

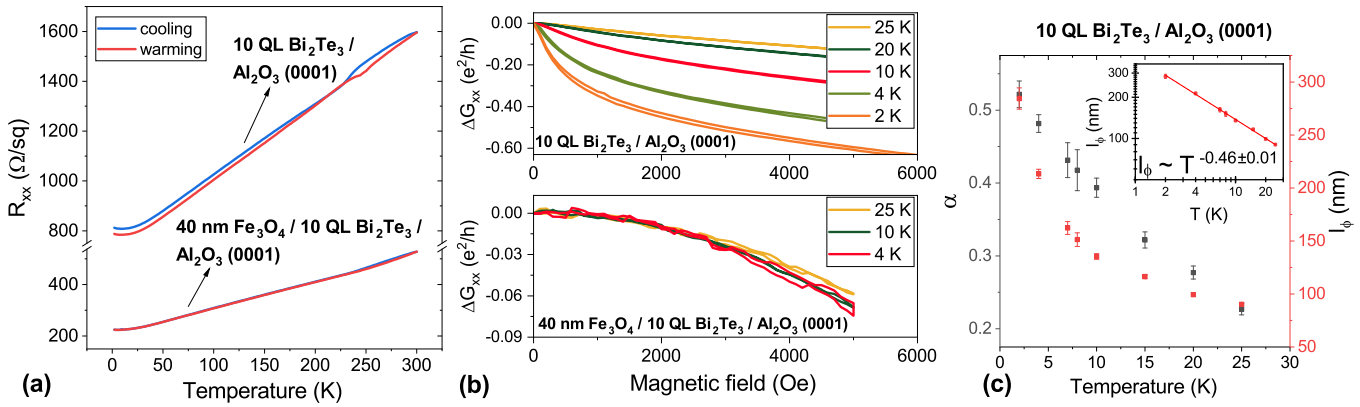

FIG. 5. (a) Sheet resistance as a function of temperature for 10 QLs of Bi_2Te_3 on Al_2O_3 (0001) and for the optimized heterostructure of 40 nm of Fe_3O_4 grown on top of 10 QLs of Bi_2Te_3. (b) Magnetoconductance for both samples. For the heterostructure, the magnetoconductance shows only a parabolic B-field dependence. (c) Dependence of the HLN fitting parameters, α and l_ϕ, for the TI grown on Al_2O_3 (0001).

The decreasing value of α with temperature has been previously reported[7,20] and is usually attributed to thermal broadening. The phase coherence length has a value of $\approx$ 285 nm at 2 K, which is similar to previous studies on TI thin films[7,11,20]. The dependence of l_ϕ with temperature is shown in the inset in Figure 5(c). Theoretically, the coherence length is proportional to $T^{-1/2}$ for the two-dimensional system and $T^{-1/3}$ for the one-dimensional system if one considers an inelastic electron-electron scattering mechanism[31]. Our fit is therefore very close to the 2D case, with $l_\phi \approx T^{-0.46\pm0.01}$.

For the magnetoconductance of the heterostructure plotted in Figure 5(b)-bottom, however, there is no apparent dependence on the temperature and the typical WAL cusp is absent. In fact, the magnetoconductance now displays only a parabolic B-field dependence. Previously reported experiments show that the WAL effect was completely quenched for 1 ML Fe deposited on Bi_2Te_3 thin films[11]. However, this behavior cannot be unambiguously attributed to a gap opening due to the proximity effect, since random magnetic scattering can cause a similar effect[19].

The latter is indeed a very plausible scenario for the heterostructure of 40 nm Fe_3O_4/10 QL Bi_2Te_3/Al_2O_3 (0001). Despite a careful optimization of the growth process, we were not able to prevent a substantial intermixing of iron and the TI layer, which has also been reported in an earlier study[14]. Such a scenario could explain a B^2-dependence of the magnetoconductance, as seen in Figure 5(b)-bottom.

B. Bi_2Te_3 on Fe_3O_4 on MgO (001)

The absence of the WAL effect in the samples described in the previous section motivated a different approach when interfacing magnetite and Bi_2Te_3. The current section reports on heterostructures of Bi_2Te_3 grown on Fe_3O_4 (001) on MgO (001). For all the films, the magnetite layer has a thickness of 30 nm, which shows a sharp RHEED pattern with the presence of Kikuchi lines and the $\left(\sqrt{2}\times\sqrt{2}\right)R45°$ surface reconstruction signature[16]. Following this, the growth of the Bi_2Te_3 layer was carried out in a two-step procedure. Attempts to grow the topological insulator layer at a substrate temperature of 160 °C in the first step led to poor crystalline quality, as can be seen in Figure 6 (a). The RHEED shows polycrystalline and island growth that does not improve even for the thicker film, with 10 QLs. The two-step procedure was then adapted, in which the first 2 QLs were grown at room temperature and, after the annealing, the subsequent QLs were grown at 220 °C. The result is displayed in Figure 6 (b). It is remarkable that even for a 2 QL film, the RHEED pattern shows streaky lines, indicative of the good crystalline order of the film. These become clearer in the 10 QL film. However, the film also displays additional streaks when compared to the TI grown on Al_2O_3 (cf. Figure 4(a)), which is an indication of the presence of multiple domains.

In order to investigate the quality of the interface between Fe_3O_4 and Bi_2Te_3, XPS measurements were performed for all the steps of the growth process. Figure 7 shows the Fe $2p$, Te $3d$ and Bi $4f$ XPS spectra. For the Fe $2p$ peak, one can observe that the signal is quite reduced when we have 2 QLs of Bi_2Te_3, and disappears for 10 QLs. This implies that a relatively uniform, closed layer of the topological insulator is indeed covering the magnetite. Regarding the Te $3d$ and Bi $4f$ core levels for the 2 QL film, a noticeable shoulder appears at higher binding energies. This indicates a reaction between the layers, compatible with the formation of Bi-O and Te-O bonds. Nevertheless, no strong signal of metallic bismuth or tellurium and bismuth oxides is visible. This is to be contrasted to what was reported in the previous section, where even for the optimized heterostructure, peaks indicative of oxides could be identified. Finally, for the

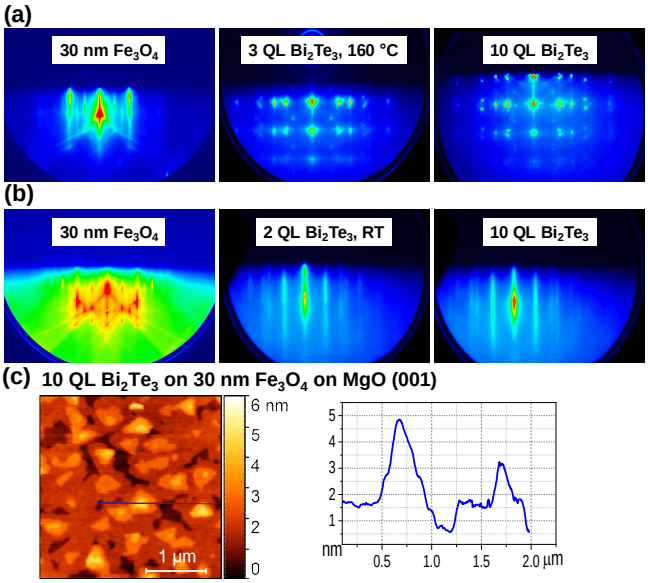

FIG. 6. RHEED patterns of the heterostructures of Bi_2Te_3 grown on 30 nm of Fe_3O_4 films where (a) the first 3 QLs of the topological insulator layer were grown at 160 °C; (b) the first 2 QLs were grown at room temperature. In both cases, the first layers were annealed at 240 °C in Te atmosphere and the following layers were grown at 220 °C. (c) Morphological characterization by AFM of 10 QLs of Bi_2Te_3 on 30 nm of Fe_3O_4 on MgO (001) grown under the conditions described in (b).

thicker film, the line shape is similar to that of the Bi_2Te_3 reference grown on Al_2O_3 (0001).

The morphological characterization performed by AFM of a 10 QL Bi_2Te_3 film grown on 30 nm Fe_3O_4 on MgO (001) is presented in Figure 6(c). Similarly to the film grown on Al_2O_3 (0001) (cf. Figure 4(c)) the pyramidal structure with steps of 1 QL-height are visible. However there are an increased number of rotated domains in-plane. This is in agreement with the RHEED measurements, which indicate an increase in the in-plane disorder of the film.

From the XRD scans, Figure 8(a), one can observe that for both the TI grown on Al_2O_3 (0001) and on 30 nm Fe_3O_4 / MgO (001), all the peaks can be identified as the (0 0 n) family plane of the Bi_2Te_3 phase or the underlying layers, implying a good orientation along the c-direction. From the in-plane ϕ-rotation scan around the (1 0 5) Bi_2Te_3 peak in Figure 8(b), however, it is possible to observe significant differences between the heterostructure and the reference sample. From the TI/Al_2O_3 (0001) scan, one can observe the predominance of one domain with three-fold symmetry and a second domain with significantly less intensity. This is to be expected for Bi_2Te_3 grown on Al_2O_3 (0001) due to the large lattice mismatch, which favors the formation of domains with 60° rotation[32]. For the TI grown on the magnetite film, on the other hand, the ϕ-scan shows a higher degree of in-plane disorder, with weak reflections occurring every 30°. The lattice mismatch and the different symmetries between Fe_3O_4 (001) and Bi_2Te_3 increase the number of rotated domains around the c-axis. The XRD results are consistent with the RHEED patterns and AFM measurements displayed in Figures 4(a,c) and 6(b,c).

Figure 9(a) shows the ARPES spectra for the two steps of growth of the TI on a magnetite film, as well as a reference spectra for 10 QLs of Bi_2Te_3 on Al_2O_3 (b). Even for nominally 2 QLs of Bi_2Te_3 the surface states are visible, albeit on top of a strong background and a visible contribution from the bulk conduction band. Thickness dependent studies on Bi_2Te_3 thin films have shown very similar results[33]. The topological features start to appear for a thickness of 2 nm, and the contribution from the bulk conduction band becomes increasingly reduced as the thickness of the film increases. This is also observable in our films and, for 10 QLs, the surface states are now clearly visible and intersect the Fermi level without any contribution from the bulk. The spectrum is similar to the reference (b) and the position of the Dirac point ($\approx$ 150 meV) does not present significant changes, indicating a conservation of the top topological surface states. Nevertheless, the spectrum regarding the heterostructure appears more blurred, which is, once again, consistent with the presence of rotated domains around the c-axis.

The temperature-dependent sheet resistance depicted in Figure 10(a) shows now the expected behavior for a parallel resistance between the layers: for high temperatures, the resistance increases as the temperature decreases, as characteristic for Fe_3O_4. At $T \approx T_V \approx 120$ K, the Verwey transition is visible in the form of a jump in the resistivity and, for $T < T_V$, the transport is dominated by the more conductive Bi_2Te_3 layer, with the upturn characteristic of topological insulators at around 10 K.

Figure 10(b) displays the magnetoconductance for a film with 10 QLs of Bi_2Te_3 on 30 nm of Fe_3O_4 on MgO (001). Contrary to the previous heterostructure (Figure 5(b)), the WAL effect is still present at low temperatures and low magnetic fields. However, a visual comparison with the TI grown on Al_2O_3 (0001) (dashed line) shows that the WAL feature is suppressed in the case of the magnetic heterostructure. The XPS results in Figure 7 suggest the presence of some chemical reaction at the interface. However, the amount is very small so that we can readily expect that the exchange coupling between Fe_3O_4 and Bi_2Te_3 layers will still be intact. Furthermore, it has been reported that WL due to bulk subbands in ultrathin films[34] and defect-induced WL[35] can occur. Based on our sample characterization, the quality of the Bi_2Te_3 layers is comparable for the Al_2O_3 and Fe_3O_4 substrates. Therefore, we rule out these effects as the main origin of the suppressed WAL, which thus should likely originate from the magnetic interaction with the Fe_3O_4 surface.

In order to understand the effect of the proximity with a magnetic layer, the HLN equation (1) was fitted to the data. The evolution of α and l_ϕ with the temperature is

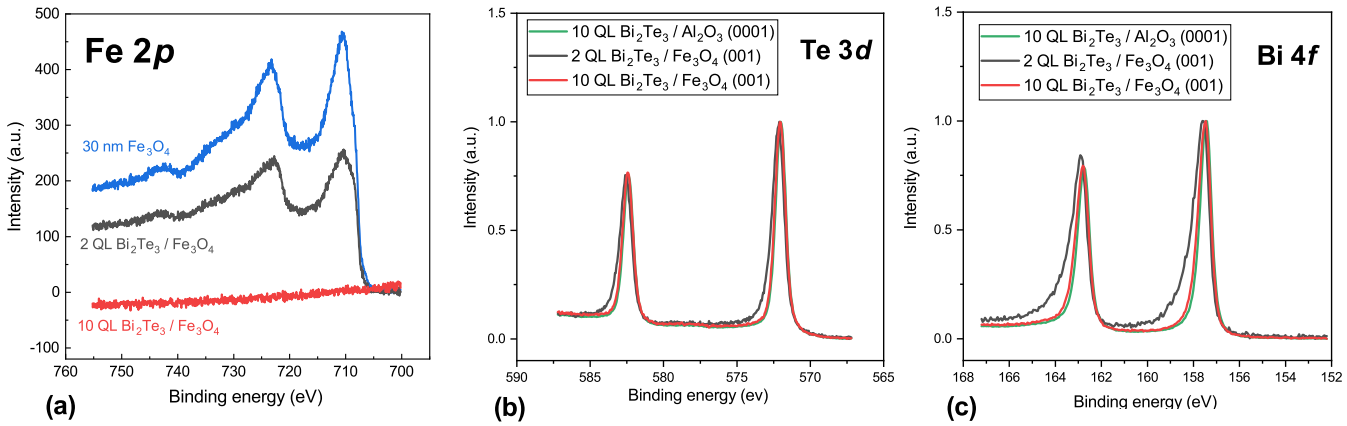

FIG. 7. XPS spectra of Fe $2p$ (a), Te $3d$ (b) and Bi $4f$ (c) core levels for each step of the growth of 10 QLs Bi_2Te_3 on 30 nm Fe_3O_4 on MgO (001). For (b) and (c), the reference spectra of 10 QLs Bi_2Te_3 on Al_2O_3 (0001) are shown in green.

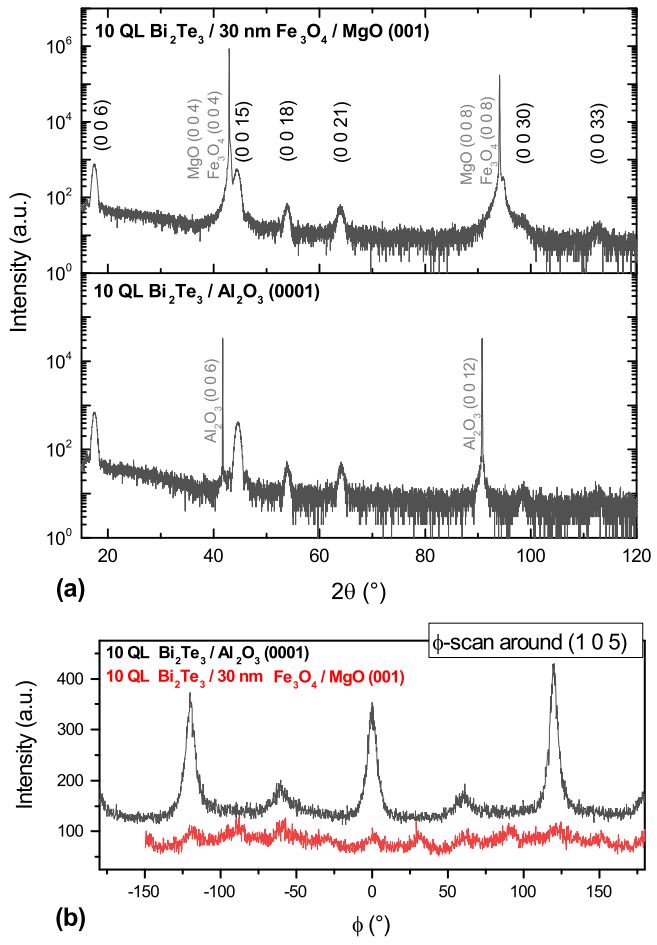

FIG. 8. (a) XRD $\theta - 2\theta$ scans of the heterostructure 10 QL Bi_2Te_3 / 30 nm Fe_3O_4 / MgO (001) (*top*) and the reference grown on Al_2O_3 (00001) (*bottom*). (b) In-plane ϕ-rotation around the (1 0 5) Bi_2Te_3 peak for the same samples. An increased in-plane disorder can be noticed for the heterostructure.

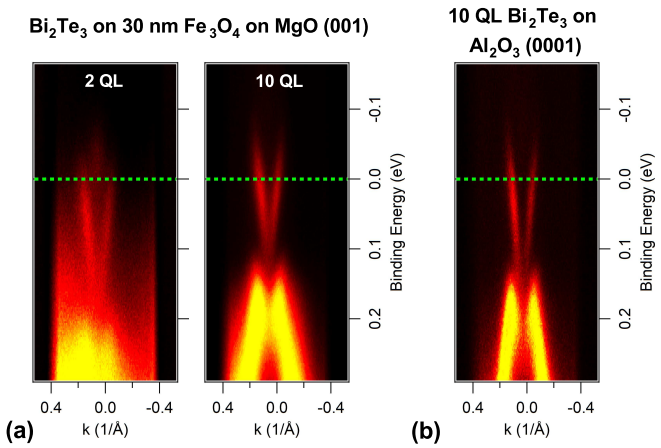

FIG. 9. *In situ* ARPES spectra of 2 QL and 10 QL Bi_2Te_3 on 30 nm Fe_3O_4 on MgO (001) (a) and spectra of a reference sample grown on Al_2O_3 (0001) (b).

presented in Figure 10(c). The strong reduction of the phase coherence length of the heterostructure ($l_\phi \approx 100$ nm at 2 K), when compared to the sample grown on a non-magnetic substrate ($l_\phi \approx 285$ nm at 2 K), can be explained by the additional magnetic scattering due to the proximity to the underlying magnetic layer. Furthermore, the dependence of l_ϕ with the temperature seems to be altered, being now described by $l_\phi \approx T^{-0.17\pm0.02}$. The decay of the coherence length of our Bi_2Te_3/Fe_3O_4 heterostructure thus deviates significantly from the theoretical model, suggesting that other scattering mechanisms, likely related to the magnetic interactions, play a crucial role. Conversely, the pre-factor α is similar to the reference sample. Reducing the thickness of the TI layer to 6 QLs leads to a suppression of α to a value of 0.39 (Ref. 36).

These results are compatible with a possible opening of a gap in the surface states at the interface between magnetite and the TI, leading to a competition between

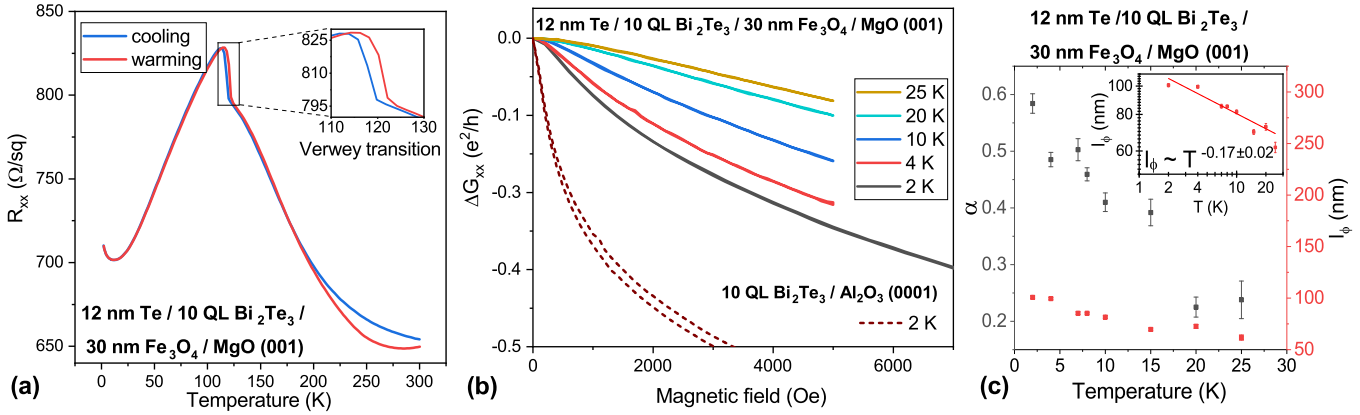

FIG. 10. (a) Sheet resistance as a function of temperature for the optimized heterostructure of 10 QL Bi_2Te_3 on top of 30 nm Fe_3O_4 on MgO (001). (b) Magnetoconductance for the same heterostructure. The data taken at 2 K for the reference sample grown on Al_2O_3 (0001) are plotted in dashed line for visual comparison. (c) Dependence of the HLN fitting parameters, α and l_ϕ, for the same heterostructure.

the WAL and WL effects[7,9,19] and ultimately resulting in reduced values of α and l_ϕ.

IV. CONCLUSIONS

From the comparative studies of the growth of heterostructures of Bi_2Te_3 and Fe_3O_4, one can conclude that, for the case of Fe_3O_4 on top of Bi_2Te_3, we encountered a very narrow growth window. Even for the best conditions, the quality of the film and the interface is less than optimal. The absence of the weak anti-localization effect in the magnetoconductance of this type of heterostructure is likely caused by the chemical and magnetic disorder across the interface.

On the other hand, we were able to obtain good quality films of Bi_2Te_3 on top of Fe_3O_4, in which the quality of both layers is comparable to our previous works on the individual materials. The good crystallinity observed by RHEED and the preservation of the top topological surface states observed by ARPES are also promising indications of the high quality of the heterostructures. Furthermore, the magnetoconductance for these heterostructures shows a suppression of the surface transport, resultant from the competition between WAL and WL effects, consistent with a gap opening due to the magnetic proximity effect.

Our work emphasizes the importance of chemically clean interfaces for the study of ferromagnetism induced by the magnetic proximity effect. The good quality of the Bi_2Te_3 / Fe_3O_4 / MgO (001) heterostructure indicates that the magnetic proximity effect can be a viable approach for the introduction of magnetic order in TI systems. The experimental realization of chemically clean interfaces together with the unique characteristics of the heterostructures that allow for a uniform magnetization of the TI pave the way for the experimental observation of the QAHE at higher temperatures than those reported in doped systems.

ACKNOWLEDGMENTS

The authors would like to thank Steffen Wirth for the valuable discussions. We would also like to thank Katharina Höfer and Christoph Becker for the skillful technical assistance and the department of Claudia Felser for the use of the thin films XRD instrument. Financial support from the DFG through Priority Program SPP-1666 Topological Insulators and the Max Planck-POSTECH-Hsinchu Center for Complex Phase Materials is gratefully acknowledged. C.N.W. acknowledges support from the Ministry of Science and Technology of Taiwan, through grant MoST 105-2112-M-007-014-MY3, and V.M.P. from the International Max Planck Research School for Chemistry and Physics of Quantum Materials (IMPRS-CPQM).

The data that support the findings of this study are available from the corresponding author upon reasonable request.

[1] L. Fu, C. L. Kane, and E. J. Mele, Physical Review Letters **98**, 106803 (2007).
[2] C.-Z. Chang, J. Zhang, X. Feng, J. Shen, Z. Zhang, M. Guo, K. Li, Y. Ou, P. Wei, L.-L. Wang, Z.-Q. Ji, Y. Feng, S. Ji, X. Chen, J. Jia, X. Dai, Z. Fang, S.-C. Zhang, K. He, Y. Wang, L. Lu, X.-C. Ma, and Q.-K. Xue, Science **340**, 167 (2013).
[3] C.-Z. Chang, W. Zhao, D. Y. Kim, H. Zhang, B. A. Assaf, D. Heiman, S.-C. Zhang, C. Liu, M. H. W. Chan, and J. S. Moodera, Nature Materials **14**, 473 (2015).
[4] M. Mogi, R. Yoshimi, A. Tsukazaki, K. Yasuda, Y. Kozuka, K. S. Takahashi, M. Kawasaki, and Y. Tokura, Applied Physics Letters **107**, 182401 (2015).
[5] M. Ye, W. Li, S. Zhu, Y. Takeda, Y. Saitoh, J. Wang, H. Pan, M. Nurmamat, K. Sumida, F. Ji, Z. Liu, H. Yang, Z. Liu, D. Shen, A. Kimura, S. Qiao, and X. Xie, Nature Communications **6**, 8913 (2015).

[6] P. Wei, F. Katmis, B. A. Assaf, H. Steinberg, P. Jarillo-Herrero, D. Heiman, and J. S. Moodera, Physical Review Letters **110**, 186807 (2013).

[7] Z. Jiang, F. Katmis, C. Tang, P. Wei, J. S. Moodera, and J. Shi, Applied Physics Letters **104**, 222409 (2014).

[8] C. Tang, C.-Z. Chang, G. Zhao, Y. Liu, Z. Jiang, C.-X. Liu, M. R. McCartney, D. J. Smith, T. Chen, J. S. Moodera, and J. Shi, Science Advances **3**, e1700307 (2017).

[9] S. R. Yang, Y. T. Fanchiang, C. C. Chen, C. C. Tseng, Y. C. Liu, M. X. Guo, M. Hong, S. F. Lee, and J. Kwo, Physical Review B **100**, 045138 (2019).

[10] L. A. Wray, S.-Y. Xu, Y. Xia, D. Hsieh, A. V. Fedorov, Y. S. Hor, R. J. Cava, A. Bansil, H. Lin, and M. Z. Hasan, Nature Physics **7**, 32 (2011).

[11] H.-T. He, G. Wang, T. Zhang, I.-K. Sou, G. K. L. Wong, J.-N. Wang, H.-Z. Lu, S.-Q. Shen, and F.-C. Zhang, Physical Review Letters **106**, 166805 (2011).

[12] J. Honolka, A. A. Khajetoorians, V. Sessi, T. O. Wehling, S. Stepanow, J.-L. Mi, B. B. Iversen, T. Schlenk, J. Wiebe, N. B. Brookes, A. I. Lichtenstein, Ph. Hofmann, K. Kern, and R. Wiesendanger, Physical Review Letters **108**, 256811 (2012).

[13] A. Polyakov, H. L. Meyerheim, E. D. Crozier, R. A. Gordon, K. Mohseni, S. Roy, A. Ernst, M. G. Vergniory, X. Zubizarreta, M. M. Otrokov, E. V. Chulkov, and J. Kirschner, Physical Review B **92**, 045423 (2015).

[14] J. Sánchez-Barriga, I. I. Ogorodnikov, M. V. Kuznetsov, A. A. Volykhov, F. Matsui, C. Callaert, J. Hadermann, N. I. Verbitskiy, R. J. Koch, A. Varykhalov, O. Rader, and L. V. Yashina, Physical Chemistry Chemical Physics **19**, 30520 (2017).

[15] E. J. W. Verwey, Nature **144**, 327 (1939).

[16] X. H. Liu, A. D. Rata, C. F. Chang, A. C. Komarek, and L. H. Tjeng, Physical Review B **90**, 125142 (2014).

[17] X. H. Liu, C. F. Chang, A. D. Rata, A. C. Komarek, and L. H. Tjeng, npj Quantum Materials **1**, 16027 (2016).

[18] K. Höfer, C. Becker, D. Rata, J. Swanson, P. Thalmeier, and L. H. Tjeng, Proceedings of the National Academy of Sciences **111**, 14979 (2014).

[19] H.-Z. Lu, J. Shi, and S.-Q. Shen, Physical Review Letters **107**, 076801 (2011).

[20] A. Kandala, A. Richardella, D. W. Rench, D. M. Zhang, T. C. Flanagan, and N. Samarth, Applied Physics Letters **103**, 202409 (2013).

[21] L. Fu, Physical Review Letters **103**, 266801 (2009).

[22] X. Liu, H.-C. Hsu, and C.-X. Liu, Physical Review Letters **111**, 086802 (2013).

[23] C. F. Chang, Z. Hu, S. Klein, X. H. Liu, R. Sutarto, A. Tanaka, J. C. Cezar, N. B. Brookes, H.-J. Lin, H. H. Hsieh, C. T. Chen, A. D. Rata, and L. H. Tjeng, Physical Review X **6**, 041011 (2016).

[24] K. Höfer, C. Becker, S. Wirth, and L. H. Tjeng, AIP Advances **5**, 097139 (2015).

[25] D. Telesca, Y. Nie, J. I. Budnick, B. O. Wells, and B. Sinkovic, Physical Review B **85**, 214517 (2012).

[26] S. Gota, E. Guiot, M. Henriot, and M. Gautier-Soyer, Physical Review B **60**, 14387 (1999).

[27] J. F. Moulder and J. Chastain, *Handbook of X-ray Photoelectron Spectroscopy: A Reference Book of Standard Spectra for Identification and Interpretation of XPS Data* (Physical Electronics Division, Perkin-Elmer Corporation, 1992).

[28] W. Eerenstein, T. T. M. Palstra, T. Hibma, and S. Celotto, Physical Review B **66**, 201101(R) (2002).

[29] S. Hikami, A. I. Larkin, and Y. Nagaoka, Progress of Theoretical Physics **63**, 707 (1980).

[30] M. Brahlek, N. Koirala, M. Salehi, N. Bansal, and S. Oh, Physical Review Letters **113**, 026801 (2014).

[31] B. L. Altshuler, A. G. Aronov, and D. E. Khmelnitsky, Journal of Physics C: Solid State Physics **15**, 7367 (1982).

[32] K. Höfer, *All in situ ultra-high vacuum study of Bi_2Te_3 topological insulator thin films*, Ph.D. thesis, Technische Universität Dresden (2016).

[33] Y.-Y. Li, G. Wang, X.-G. Zhu, M.-H. Liu, C. Ye, X. Chen, Y.-Y. Wang, K. He, L.-L. Wang, X.-C. Ma, H.-J. Zhang, X. Dai, Z. Fang, X.-C. Xie, Y. Liu, X.-L. Qi, J.-F. Jia, S.-C. Zhang, and Q.-K. Xue, Advanced Materials **22**, 4002 (2010).

[34] H.-Z. Lu and S.-Q. Shen, Physical Review B **84**, 125138 (2011).

[35] K. Banerjee, J. Son, P. Deorani, P. Ren, L. Wang, and H. Yang, Physical Review B **90**, 235427 (2014).

[36] V. M. Pereira, S. G. Altendorf, C. E. Liu, S. C. Liao, A. C. Komarek, M. Guo, H. J. Lin, C. T. Chen, M. Hong, J. Kwo, L. H. Tjeng, and C. N. Wu, Physical Review Materials, accepted (2020).